Studies on the Three-Dimensional Temperature Transients in the Canine Prostate During Transurethral Microwave Thermal Therapy

Jing Liu
School of Mechanical Engineering,
Purdue University,
West Lafayette, IN 47907-1288

Liang Zhu
Department of Mechanical Engineering,
University of Maryland at Baltimore County,
Baltimore, MD 21250

Lisa X. Xu[1]
School of Mechanical Engineering,
Department of Biomedical Engineering,
Purdue University,
West Lafayette, IN 47907-1288
e-mail: lxu@ecn.purdue.edu

Thermal therapy of benign prostatic hyperplasia requires accurate prediction of the temperature distribution induced by the heating within the prostatic tissue. In this study, the Pennes bioheat transfer equation was used to model the transient heat transfer inside the canine prostate during transurethral microwave thermal therapy. Incorporating the specific absorption rate of microwave energy in tissue, a closed-form analytical solution was obtained. Good agreement was found between the theoretical predictions and in-vivo experimental results. Effects of blood perfusion and the cooling at the urethral wall on the temperature rise were investigated within the prostate during heating. The peak intraprostatic temperatures attained by application of 5, 10, or 15 W microwave power were predicted to be 38°C, 41°C, and 44°C. Results from this study will help optimize the thermal dose that can be applied to target tissue during the therapy.
[S0148-0731(00)01004-9]

Keywords: Prostate, Thermal Therapy, Bioheat Transfer, Temperature, Blood Perfusion

Introduction

Localized transurethral thermal therapy has been widely used as a nonsurgical modality for treatment of benign prostatic hyperplasia [1–8]. One of the critical issues in clinical application is to heat and cause coagulation necrosis effectively in target tissue while simultaneously preserving the surrounding healthy tissue, especially the prostatic urethra and rectum. This requires administration of an optimal thermal dose that can induce the desired three-dimensional tissue temperature distributions in the prostate during the therapy. Although some thermal analyses have been previously conducted [9–15], none of these studies utilized the analytical approach to solving the transient three-dimensional temperature field. The analytical approach can accurately provide point-by-point tissue temperature mapping during heating. The one- or two-dimensional models are generally not good enough for accurate predictions of the real thermal fields generated by the three-dimensional asymmetric microwave heating.

The canine prostate is similar to that of a human being in development of prostatic hyperplasia and has been commonly used as an alternative to examine treatment efficacy given its similarity [16,17]. Figure 1 shows a general appearance of the canine prostate. Its vascular cast was obtained by injecting blue methylmethacrylate plastic (Mercox CI-2B) through the internal iliac artery. In each lobe, the paired prostatic artery and vein run along its lateral surface toward the front, and branch into smaller vessels spreading away like a brush. The cast was sliced either perpendicular or parallel to the prostatic urethra. All slices were corroded in a warm saturated KOH and methanol (80 percent/20 percent vol.) solution. Figure 2 shows both the cross-sectional and longitudinal slices after the tissue was digested. As shown in Fig. 2(*a*), tributaries of approximately 140 μm diameter and 7 mm length branch off the large capsular vessels of 820 μm diameter and penetrate radially into the parenchyma. The dimensions of the vessels were average values of measurements made in three canine prostates. Near the center, numerous vessels form the artery-venous plexus that surrounds the prostatic urethra (see Fig. 2(*b*)). These vessels are typically of 280 μm diameter. For modeling purposes, a schematic cross-sectional view of the canine prostatic vasculature is given in Fig. 3. In parenchyma, if one views the prostatic arteries as the arcuate arteries at the corticomedullary junction in the pig kidney, then the radial tributaries supplying the glandular tissue are distributed toward the urethra similarly to the radial arteries projecting toward the kidney surface. Since tributaries are about 140 μm in diameter, the Pennes bioheat equation can be used for heat transfer modeling in the parenchyma tissue with good agreement [18].

Surrounding the prostatic urethra, the periurethral tissue takes up approximately 10 percent of the total cross section. The transurethral thermal therapy (T3) catheter (Urologix, Inc., Minneapolis, MN) was used as the heating apparatus in the present study. Once the T3 catheter was inserted, the tissue region was compressed and vessels were forced to be closer to each other. Their thermal effects were thus considered collectively and combined into the boundary condition at the urethra wall. The three-dimensional specific absorption rate of microwave energy in tissue induced by the catheter was recently quantified [12]. Incorporating the volumetric heating, the Pennes equation was used to develop a heat transfer model in the prostatic tissue. A closed-form analytical solution to the three-dimensional Pennes equation was obtained using the Green's function method. This solution could be used to predict the evolution of temperature distribution in tissue during heating accurately. The validity of the model was examined by comparing the predicted to the experimentally measured temperatures at various prostatic locations during the microwave heating. The convective effect of blood perfusion and the chilled water running between the microwave antenna and the urethral wall were also studied. The parametric studies would provide some insights into the controlling factors of the temperature

[1]Corresponding author.

Contributed by the Bioengineering Division for publication in the JOURNAL OF BIOMECHANICAL ENGINEERING. Manuscript received by the Bioengineering Division February 22, 1999; revised manuscript received March 22, 2000. Associate Technical Editor: J. J. McGrath.

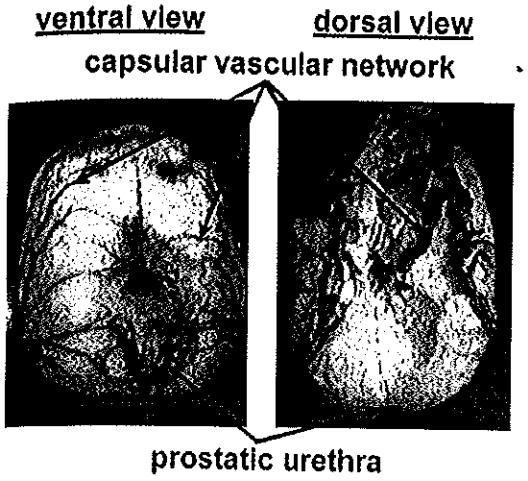

Fig. 1 Canine prostate and its capsular vascular network: (*a*) half cross-sectional slice; (*b*) longitudinal section (enlarged)

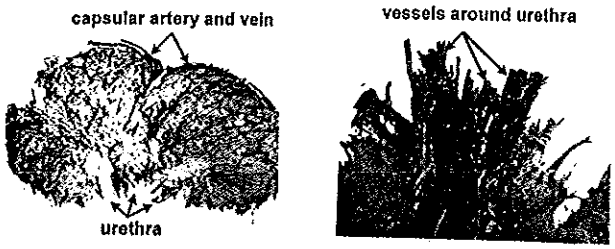

Fig. 2 Canine prostatic vasculature

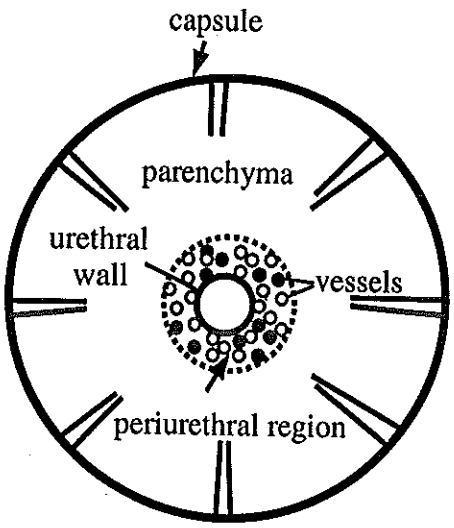

Fig. 3 Schematic cross section of the canine prostatic tissue and vessels: (*a*) prostate and catheter; (*b*) catheter (enlarged)

distributions in the prostatic tissue during transurethral microwave heating, which will help optimize the thermal dose to be used for the therapy.

Heat Transfer Modeling

Geometric presentation of the prostate with the inserted T3 catheter is shown in Fig. 4. It is modeled as a cylinder of 3.4 cm in diameter and 3 cm in length with a constant temperature T_∞ at the surface, which is close to the body core temperature. The catheter is represented by the inner cylinder. The induced volumetric heating in tissue is [12]

$$q'''(r,\theta,z)=C_t Q\frac{[2\varepsilon(r-s\cos\theta)+(N-2)]e^{-2\varepsilon(r-s\cos\theta)}}{(r-s\cos\theta)^N}\times e^{-(z-L/2)^2/z_0^2} \tag{1}$$

It takes into account the attenuation of the electromagnetic field in the radial direction and the Gaussian distribution along the axial direction. Q is the applied microwave power (W) and C_t is a proportional constant. ε is the microwave attenuation constant in tissue. z_0 is the critical axial decay length along the catheter and L is the total length of the prostate. The parameters N, z_0, ε in Eq. (1) are given as

$$N=2.2,\ z_0=18.5\,(\text{mm}),\ \varepsilon=0.0413\,\text{mm}^{-1}$$

where the proportional parameter C_t in the prostatic tissue is $0.00657\,\text{mm}^{-0.8}$ [10]. Practically, the microwave antenna is located with an offset s from the geometric center to produce an asymmetric microwave field, which can prevent overheating of the rectum. The chilled water at a given temperature flows between the antenna and the inner catheter wall.

The Pennes equation for the three-dimensional temperature field in the prostate is applied as

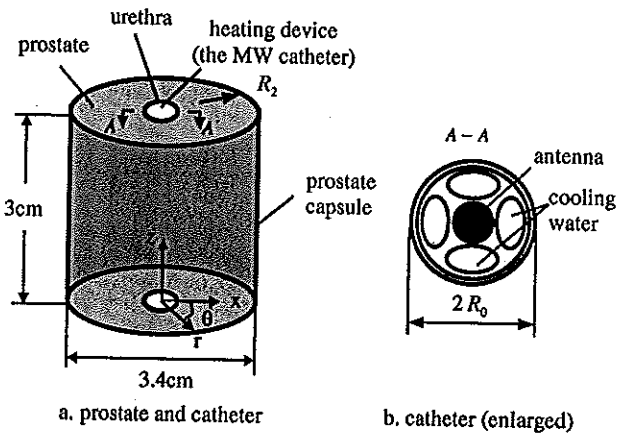

Fig. 4 Three-dimensional configuration of the prostate under microwave heating

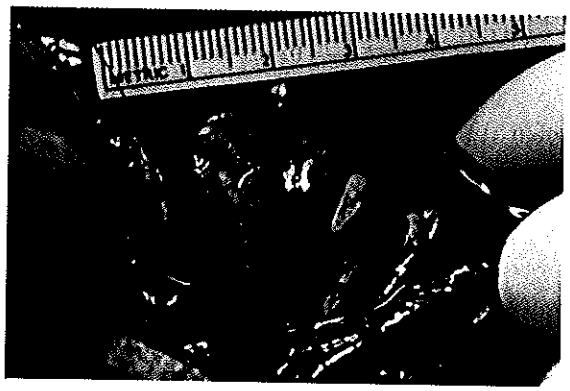

Fig. 5 Temperature and blood perfusion measurement in the canine prostate

$$k\frac{1}{r}\frac{\partial}{\partial r}\left(r\frac{\partial T}{\partial r}\right)+k\frac{1}{r^2}\frac{\partial^2 T}{\partial \theta^2}+k\frac{\partial^2 T}{\partial z^2}+\omega_b\rho_b c_b(T_a-T)+q_m+q'''=\rho c\frac{\partial T}{\partial t} \tag{2}$$

where ρ, c, and k denote density, specific heat, and thermal conductivity of tissue, respectively; ρ_b, c_b are density, specific heat of blood; ω_b is the blood perfusion rate; T_a is the supplying arterial blood temperature; q_m is the volumetric metabolic heat. To obtain an analytical solution, all these parameters were assumed to be uniform throughout the prostate and remained constant, except for ω_b, which varies with the heat power.

Our analyses mainly focus on temperature elevations in parenchyma induced by the heating. The cooling effect from the chilled water running inside the catheter is modeled by an overall convection coefficient h. The external boundary at the capsule is prescribed as the body core temperature T_∞. Therefore, one has

$$k\frac{\partial T}{\partial r}=h(T-T_f) \text{ at } r=R_0 \tag{2a}$$

$$T=T_\infty \text{ at } r=R_2 \tag{2b}$$

where R_0 and R_2 are the urethra and prostate radius, respectively. T_f is the coolant temperature. Considering the Gaussian distribution of microwave power deposition along the z direction, adiabatic conditions can be used at two ends of the prostate,

$$k\frac{\partial T}{\partial z}=0, \quad z=0, \quad L \tag{2c}$$

The initial temperature is

$$T(r,\theta,z,0)=T_0(r,\theta,z), \quad t=0 \tag{2d}$$

Using transformation

$$T=\Delta+T_\infty+(T_\infty-T_f)\frac{\ln(r/R_2)}{\ln(R_2/R_0)+k/(hR_0)} \tag{3}$$

one can rewrite Eqs. (2)–(2d) as

$$\frac{1}{r}\frac{\partial}{\partial r}\left(r\frac{\partial \Delta}{\partial r}\right)+\frac{1}{r^2}\frac{\partial^2\Delta}{\partial\theta^2}+\frac{\partial^2\Delta}{\partial z^2}-\frac{\omega_b\rho_b C_b\Delta}{k}+\frac{q^*(r,\theta,z)}{k}=\frac{1}{\alpha}\frac{\partial\Delta}{\partial t} \tag{4}$$

$$k\frac{\partial\Delta}{\partial r}=h\Delta, \quad r=R_0 \tag{4a}$$

$$\Delta=0, \text{ at } \quad r=R_2 \tag{4b}$$

$$k\frac{\partial\Delta}{\partial z}=0, \quad z=0,L \tag{4c}$$

$$\Delta(r,\theta,z,0)=F(r,\theta,z), \quad t=0 \tag{4d}$$

where

$$q^*(r,\theta,z)=q'''(r,\theta,z)+q_m+\omega_b\rho_b C_b\times\left[T_a-T_\infty-(T_\infty-T_f)\frac{\ln(r/R_2)}{\ln(R_2/R_0)+k/(hR_0)}\right] \tag{4e}$$

$$F(r,\theta,z)=T_0(r,\theta,z)-T_\infty-(T_\infty-T_f)\frac{\ln(r/R_2)}{\ln(R_2/R_0)+k/(hR_0)} \tag{4f}$$

The Green's function method is particularly useful in solving boundary value problems with heat sources/sinks and nonhomogeneous boundary and initial conditions. Its detailed description can be found in [19]. Thus, if the Green's function is available, the transient temperature field can be easily constructed. To solve the Green's function, the following auxiliary problem is considered for the same region:

$$\frac{1}{r}\frac{\partial}{\partial r}\left(r\frac{\partial W}{\partial r}\right)+\frac{1}{r^2}\frac{\partial^2 W}{\partial\theta^2}+\frac{\partial^2 W}{\partial z^2}-\frac{\omega_b\rho_b C_b W}{k}=\delta(r-\xi)\delta(\theta-\eta)\delta(z-\lambda)\delta(t-\tau)+\frac{1}{\alpha}\frac{\partial W}{\partial t} \tag{5}$$

$$k\frac{\partial W}{\partial r}=hW, \quad r=R_0 \tag{5a}$$

$$W=0, \quad \text{at } r=R_2 \tag{5b}$$

$$W(r,\theta=\eta+\theta_1,z,t)=W(r,\theta=\eta-\theta_1,z,t) \tag{5c}$$

$$W(r,\theta,z,0)=0, \quad t=0 \tag{5d}$$

$$\frac{\partial W}{\partial z}=0, \quad z=0,L \tag{5e}$$

where $W(r,\theta,z,0)=0$, $t=0$ obeys the causality requirement that the Green's function G be zero for $t<\tau$; Eq. (5c) is used to reflect the symmetrical distribution of temperature about the heat source which is at the angular position η, while θ_1 is any angular deviation from η.

Assume that

$$W(r,\theta,z,t;\xi,\eta,\lambda,\tau)=\sum_{m=0}^{\infty}\Theta_m(\theta)W_m(r,z,t;\xi,\lambda,\tau) \tag{6}$$

where Θ_m is found from

$$\frac{d^2\Theta_m}{d\theta^2}=-m^2\Theta_m(\theta), \quad m=0,1,2,\ldots,\infty \tag{7}$$

Considering the symmetric temperature distribution about the heat source, Θ_m should satisfy,

$$\Theta_m(\theta=\eta+\theta_1)=\Theta_m(\theta=\eta-\theta_1) \tag{7a}$$

The general solution for Eq. (7) is,

$$\Theta_m(\theta)=A\cos[m(\theta-\eta)]+B\sin[m(\theta-\eta)] \tag{7b}$$

Substituting Eq. (7b) into Eq. (7a), the eigenfunction $\Theta_m(\theta)$ is obtained as:

$$\Theta_m(\theta)=\cos[m(\theta-\eta)], \quad m=0,1,2,\ldots,\infty \tag{8}$$

Substituting Eqs. (6) and (8) into Eq. (5) leads to

$$\sum_{m=0}^{\infty}\left[\frac{1}{r}\frac{\partial}{\partial r}\left(r\frac{\partial W_m}{\partial r}\right)-\frac{m^2}{r^2}W_m+\frac{\partial^2 W_m}{\partial z^2}-\frac{\omega_b\rho_b C_b W_m}{k}\right]\times\cos[m(\theta-\eta)]=\delta(r-\xi)\delta(\theta-\eta)\delta(z-\lambda)\delta(t-\tau)+\sum_{m=0}^{\infty}\frac{1}{\alpha}\frac{\partial W_m}{\partial t}\cos[m(\theta-\eta)] \tag{9}$$

Multiplying both sides of Eq. (9) by $\Theta_m(\theta)=\cos[m(\theta-\eta)]$ and integrating it from $-\pi<\theta<\pi$, one obtains,

$$\frac{1}{r}\frac{\partial}{\partial r}\left(r\frac{\partial W_0}{\partial r}\right)+\frac{\partial^2 W_0}{\partial z^2}-\frac{\omega_b\rho_b C_b W_0}{k}$$

$$=\frac{1}{2\pi}\delta(r-\xi)\,\delta(z-\lambda)\,\delta(t-\tau)+\frac{1}{\alpha}\frac{\partial W_0}{\partial t},\quad m=0 \tag{10a}$$

$$\frac{1}{r}\frac{\partial}{\partial r}\left(r\frac{\partial W_m}{\partial r}\right)-\frac{m^2}{r^2}W_m+\frac{\partial^2 W_m}{\partial z^2}-\frac{\omega_b\rho_b C_b W_m}{k}$$

$$=\frac{1}{\pi}\delta(r-\xi)\,\delta(z-\lambda)\,\delta(t-\tau)+\frac{1}{\alpha}\frac{\partial W_m}{\partial t},\quad m=1,2,3,\ldots \tag{10b}$$

Similarly, assume that

$$W_m(r,z,t;\xi,\lambda,\tau)=\sum_{n=0}^{\infty}R_n(r)Z_n(z,t;\xi,\lambda,\tau) \tag{11}$$

where $R_n(r)$ satisfies,

$$\frac{1}{r}\frac{\partial}{\partial r}\left(r\frac{\partial R_n(r)}{\partial r}\right)-\frac{m^2}{r^2}R_n(r)-\frac{\omega_b\rho_b C_b}{k}R_n(r)=-\mu_n^2R_n(r) \tag{12}$$

$$k\frac{\partial R_n(r)}{\partial r}=hR_n(r),\quad r=R_0 \tag{12a}$$

$$R_n(r)=0,\quad \text{at } r=R_2 \tag{12b}$$

The eigenfunction $R_n(r)$ is obtained as

$$R_n(r)=J_m(\mu_n^*r)+A_nN_m(\mu_n^*r) \tag{13}$$

where

$$A_n=-J_m(\mu_n^*R_2)/N_m(\mu_n^*R_2) \tag{14}$$

$$k[J_m'(\mu_n^*R_0)+A_nN_m'(\mu_n^*R_0)]=h[J_m(\mu_n^*R_0)+A_nN_m(\mu_n^*R_0)] \tag{15}$$

Here J_m and N_m are the Bessel functions of the first kind and the second kind, respectively. The coefficient A_n and the eigenvalue μ_n^* are determined by Eq. (14) and (15). μ_n^* are the positive roots of Eq. (15). μ_n can be calculated from

$$\mu_n=\sqrt{\mu_n^{*2}+\frac{\omega_b\rho_b C_b}{k}} \tag{15a}$$

Similarly, substituting Eqs. (11) and (13) into Eq. (10), then multiplying both sides of Eq. (10) by $rR_n(r)$ and integrating it from $R_0\leqslant r\leqslant R_2$, one obtains

$$Z_n''(z,t;\xi,\lambda,\tau)-\mu_n^2Z_n(z,t;\xi,\lambda,\tau)$$

$$=F_{mn}(\xi)\,\delta(z-\lambda)\,\delta(t-\tau)+\frac{1}{\alpha}\frac{\partial Z_n(z,t;\xi,\lambda,\tau)}{\partial t} \tag{16}$$

where $F_{mn}(\xi)$ is expressed by

$$F_{mn}=\frac{\xi[J_0(\mu_n^*\xi)+A_nN_0(\mu_n^*\xi)]}{2\pi}\Big/\int_{R_0}^{R_2}r[J_0(\mu_n^*r)+A_nN_0(\mu_n^*r)]^2dr,\quad m=0$$

$$F_{mn}=\frac{\xi[J_m(\mu_n^*\xi)+A_nN_m(\mu_n^*\xi)]}{\pi}\Big/\int_{R_0}^{R_2}r[J_m(\mu_n^*r)+A_nN_m(\mu_n^*r)]^2dr,\quad m=1,2,3,\ldots,\infty \tag{17}$$

Finally, we assume that

$$Z_n(z,t;\xi,\lambda,\tau)=\sum_{l=0}^{\infty}Y_l(z)\Pi_l(t;\xi,\lambda,\tau) \tag{18}$$

where $Y_l(z)$ satisfies

$$Y_l''(z)-\mu_n^2Y_l(z)=-\beta_l^2Y_l(z) \tag{19}$$

$$\frac{dY_l}{dz}=0,\quad z=0,L \tag{19a}$$

One gets eigensolutions as

$$Y_l(\gamma_l,z)=\cos(\gamma_lz),\quad l=0,1,2,\ldots \tag{20}$$

where

$$\gamma_l^2=\beta_l^2-\mu_n^2 \tag{21}$$

The norm to this equation is

$$N(\gamma_l)=\begin{cases}L, & l=0\\ L/2, & l=1,2,3\ldots\end{cases} \tag{22}$$

The eigenvalues are positive roots of

$$\sin(\gamma_lL)=0,\ l=0,1,2,\ldots. \tag{23}$$

where $\gamma_l=l\pi/L$, $l=0,1,2,3\ldots.$ β_l can thus be found to be $\beta_l^2=\gamma_l^2+\mu_n^2$, $l=0,1,2,3\ldots.$ Substituting Eqs. (18) and (20) into Eq. (16), multiplying both sides of Eq. (16) by $\cos(\gamma_lz)$ and integrating from $0\leqslant z\leqslant L$, one obtains

$$-L\beta_0^2\Pi_0(t;\xi,\lambda,\tau)=F_{mn}(\xi)\,\delta(t-\tau)+\frac{L}{\alpha}\frac{\partial\Pi_l(t;\xi,\lambda,\tau)}{\partial t},\quad l=0 \tag{24a}$$

$$-\beta_l^2\frac{L}{2}\Pi_l(t;\xi,\lambda,\tau)=F_{mn}(\xi)\cos(\gamma_l\lambda)\,\delta(t-\tau)+\frac{1}{\alpha}\frac{\partial\Pi_l(t;\xi,\lambda,\tau)}{\partial t}\frac{L}{2},\quad l=1,2,\ldots \tag{24b}$$

with the initial condition: $\Pi_l(0;\xi,\lambda,\tau)=0$ based on Eq. (5*d*).

Using the transformation given in [19] and applying the property of delta function $f(t)\,\delta(t-\tau)=f(\tau)\,\delta(t-\tau)$, the solution of Eq. (24), subject to the initial condition, is obtained as

$$\Pi_0(t;\xi,\lambda,\tau)=-e^{-\alpha\beta_0^2t}\int_0^t e^{\alpha\beta_0^2t'}\cdot\frac{\alpha F_{mn}(\xi)\,\delta(t'-\tau)}{L}dt'$$

$$=-e^{-\alpha\beta_0^2(t-\tau)}\frac{\alpha F_{mn}(\xi)H(t-\tau)}{L},\quad l=0 \tag{25a}$$

$$\Pi_l(t;\xi,\lambda,\tau)=-e^{-\alpha\beta_l^2t}\int_0^t e^{\alpha\beta_l^2t'}\cdot\frac{2\alpha F_{mn}(\xi)\cos(\gamma_l\lambda)\,\delta(t'-\tau)}{L}dt'$$

$$=-e^{-\alpha\beta_l^2(t-\tau)}\frac{2\alpha F_{mn}(\xi)\cos(\gamma_l\lambda)H(t-\tau)}{L},\quad l=1,2,\ldots \tag{25b}$$

where $H(t-\tau)$ is a heavy-side unit step function which has property of $dH(t)/dt = \delta(t)$, and

$$H(t)=\begin{cases}1 & for \quad t>0\\ 0 & for \quad t\leqslant 0\end{cases}$$

Substituting Eqs. (8), (11), (13), (18), and (25) into Eq. (6), the following expression for the Green's function is obtained:

$$W(r,\theta,z,t;\xi,\eta,\lambda,\tau) = -\sum_{m=0}^{\infty}\sum_{n=0}^{\infty}\sum_{l=0}^{\infty}[J_m(\mu_n^* r)+A_n N_m(\mu_n^* r)]\cos[m(\theta-\eta)] \times\cos(\gamma_l z)e^{-\alpha\beta_l^2(t-\tau)}\frac{\kappa\alpha F_{mn}(\xi)\cos(\gamma_l\lambda)H(t-\tau)}{L} \quad (26)$$

where $\kappa=1$ when $l=0$, and $\kappa=2$ when $l=1,2,3,\ldots$. Finally, the temperature field is constructed as

$$\Delta(r,\theta,z,t)=\int_0^t d\tau\int_{R_0}^{R_2}\int_{-\pi}^{\pi}\int_0^L\frac{-q^*(\xi,\eta,\lambda)}{k}\cdot W(r,\theta,z,t;\xi,\eta,\lambda,\tau)d\xi d\eta d\lambda + \int_{R_0}^{R_2}\int_{-\pi}^{\pi}\int_0^L\frac{-W(r,\theta,z,t;\xi,\eta,\lambda,0)\cdot F(\xi,\eta,\lambda)d\xi d\eta d\lambda}{\alpha} \quad (27)$$

where $F(r,\theta,z)$ is given in Eq. (4*f*).

Equation (27) was solved using multiple integration method provided by standard FORTRAN subroutines called from the FORTRAN bank in the university UNIX environment. The commercial package is also capable of solving the temperature field numerically.

Results

Model Validation. To validate this model, theoretical predictions were compared with one set of experimental measurements made in the canine prostate during microwave heating delivered by the T3 catheter. As shown in Fig. 5, temperature mapping was performed using thermistor bead microprobes (0.3 mm diameter) inserted in the prostatic tissue. Also, the thermal conductivity and blood perfusion in the prostate were measured using the thermal pulse decay (TPD) technique as described in [20]. Errors associated in thermistor bead placement and temperature measurements were discussed in detail in [21]. A constant $k=0.5$W/m·°C and the corresponding average blood perfusions at each individual heating levels were obtained. The metabolic heat is negligible compared with the microwave heating. The other parameters applied are: $\rho=\rho_b=1000$ kg/m^3, $c=c_b=4200$ J/kg·°C [22].

Baseline temperatures were found to be fairly uniform and close to the body core temperature $T_\infty=34.27$·°C before the microwave heating was turned on, along with the chilled water. As shown in Fig. 6, after heating at the 5 W level for thirty minutes, the temperature field reached a new steady state at which blood perfusion measurements were taken using the TPD technique. This procedure was repeated at the 10 W heating level. Temperatures measured at three probe locations within the prostate are presented by the solid lines. The theoretical predictions from Eq. (27) were obtained using uniform perfusion rates of $\omega_b=0.004$ ml/s/ml and $\omega_b=0.0075$ ml/s/ml measured at the 5 W and 10 W level, respectively in [23]. In general, the theoretical and experimental results agree well. At the beginning of the 10 W heating, the prediction appears to be a little higher than the measurement. This can be in part attributed to the constant perfusion rate used throughout the prostate in the present modeling. In reality, blood flow increases gradually with tissue temperature until it reaches a new steady state. As shown in Fig. 6, it takes less than 20 minutes to reach steady state at each heating level. For shorter time heating protocol, the accuracy of the analytical solution can be improved if regional variation of the blood perfusion rate is available.

Parametric Studies. Figure 7 depicts the calculated spatial temperature distribution at steady state under 5 W heating. The measured baseline blood perfusion $\omega_b=0.004$ ml/s/ml was used in the calculation. A nearly uniform temperature distribution can be found along the angular (θ) direction except for that at $\theta=0$ deg, which corresponds to the offset of the MW antenna from the geometric center of the catheter. Here, as expected, the tempera-

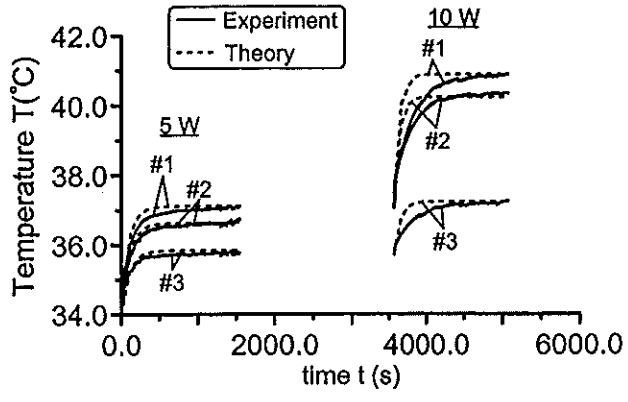

Fig. 6 Comparison of the theoretical and experimental temperature responses at various probe locations (r,θ,z: #1:0.01 m, 126.9 deg, 0.015 m; #2: 0.009 m, 160 deg, 0.013 m; #3: 0.0125 m, 135.0 deg, 0.011 m)

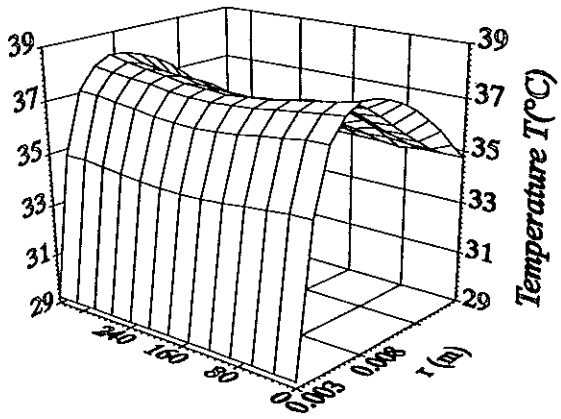

Fig. 7 Steady-state temperature distribution in the midplane ($z=0.015$ m) during 5 W heating

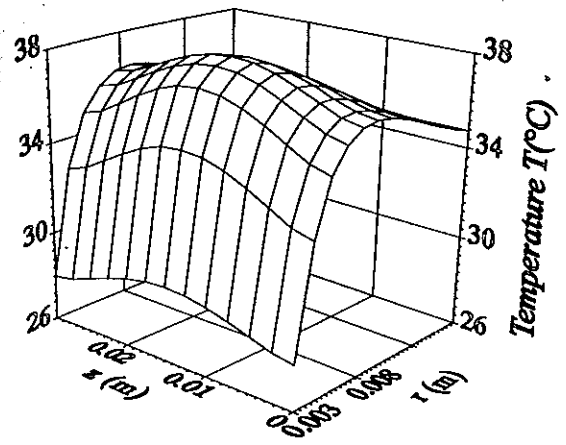

Fig. 8 Steady-state temperature distribution at $\theta=0$ deg during 5 W heating

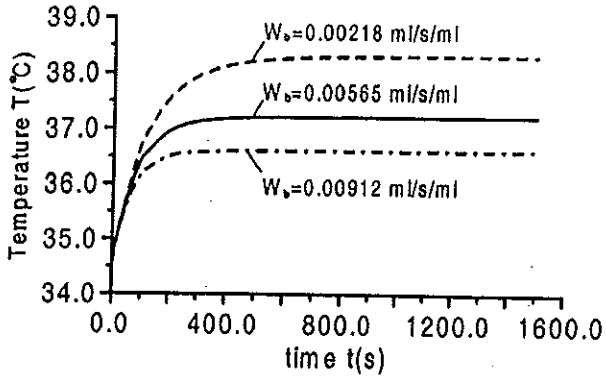

Fig. 9 Temperature profile at $r=0.008$ m, $\theta=0$, $z=0.015$ m with respect to the perfusion rate

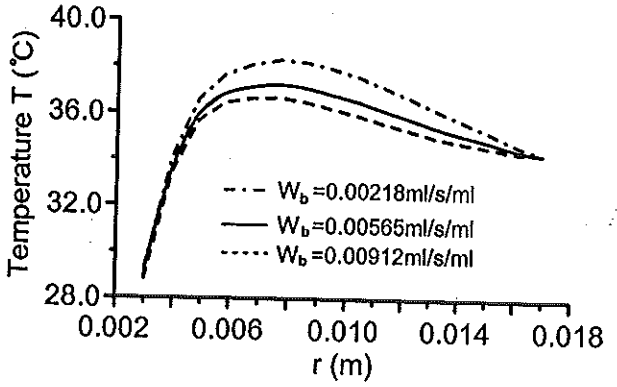

Fig. 10 Perfusion-dependent radial steady-state temperature distribution at ($\theta=0$, $z=0.015$ m) under 5 W heating

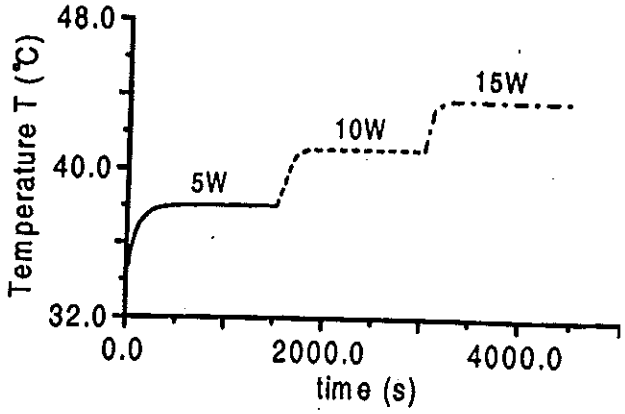

Fig. 11 Transient temperature elevation at $r=0.008$ m, $\theta=0$, $z=0.015$ m under continuous heating

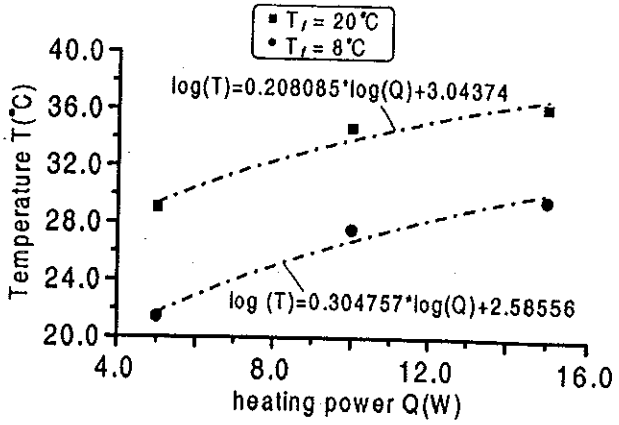

Fig. 12 Influence of the chilled water temperature on the urethral wall temperature ($r=0.003$ m, $\theta=0$, $z=0.015$ m)

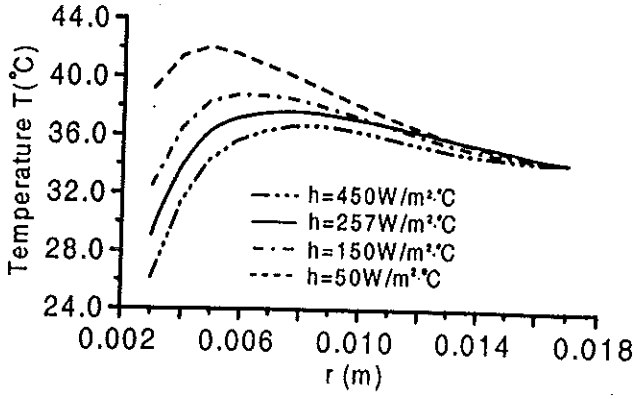

Fig. 13 Steady-state temperature distributions at ($\theta=0$, $z=0.015$ m) under 5 W heating with different convection coefficients

ture appears to be slightly high. Its distribution in the $r-z$ coordinates is given in Fig. 8. Due to the combined contribution of the MW heating, blood perfusion, and forced convection at the urethral wall, the highest temperature occurs at the radial distance $r=7.7$ mm from the center, which is consistent with that measured in [5]. The Gaussian distribution along the z direction primarily results from the MW heating pattern.

In clinical practices, it is desirable to know the temperature rise rate during the thermal therapy. Figure 9 shows the transient temperature predictions under various perfusions within the normal range at the point $r=0.008$ m, $\theta=0$, $z=0.015$ m, near where the maximal temperature occurs as mentioned above. The larger the blood perfusion, the lower the temperature increase, and the faster the tissue temperature will reach steady state. Changes in perfusion yield different radial temperature distributions at steady state as shown in Fig. 10. The resulting variation in the magnitude of temperature elevation is evident, while there exists a small shift of the location where the maximum temperature occurs in the radial direction. This reveals that the MW heating coupled with the convection effect of the chilled water on tissue heat transfer is predominant compared to that of blood perfusion.

For treatment planning, knowledge of the maximum temperature elevation induced at each individual heating level is of interest. Figure 11 shows the simulated temperature responses at the location where the maximum temperature occurs. The average perfusion rates of $\omega_b = 0.004$ ml/s/ml, $\omega_b = 0.0075$ ml/s/ml, and $\omega_b = 0.01517$ ml/s/ml from [23] were used for the 5 W, 10 W, and 15 W heating, respectively. After its initial rise, the temperature stabilizes at 38° under the 5 W heating. Subsequent heating at the 10 W level increases it to 41.1° and then to 44° at the 15 W level. To reach the tissue necrosis temperature of 45°, higher heating power is required. As a consequence, thermal damage may be induced in the urethral wall. Therefore, the maximal urethral wall temperature reached at each heating level is of interest. As shown in Fig. 12, with the chilled water temperature at either 8°C or 20°C running within the T3 catheter, the maximal urethral wall temperature does not exceed 40°C even if the heating power is raised to 20W. Clearly, the chilled water provides an effective protection of the prostatic urethral wall. As investigated in [24], the overall heat transfer coefficient (h) is insensitive to the water temperature. However, if the catheter wall were made of more conductive material instead of the silicon rubber used in the T3 catheter, then h would be more sensitive to the flow conditions. As illustrated in Fig. 13, when h becomes smaller, the location of the maximal tissue temperature moves toward the urethra wall and its magnitude is increased. Overall, the combined effect of the chilled fluid temperature and flow rate can be adjusted to optimize the deposition of thermal dose in target tissue during the therapy.

Discussion and Conclusions

In this paper, the Pennes bioheat transfer equation was used to model the three-dimensional transient heat transfer inside the canine prostate during transurethral microwave thermal therapy. The analytical solution obtained was found to be in good agreement with the in-vivo experimental results. Effects of blood perfusion and the cooling at the urethral wall on the maximum temperature rise within the prostate have been investigated. The analytical solution presented in this paper can be used to predicate the evolution of the detailed temperature within the prostate accurately during transurethral thermal therapy. The solution can serve as a benchmark for validating numerical studies involving more complex modeling aspects for prediction of temperature in in-vivo tissues. It can also be used to solve the inverse problem for spatial and temporal variations of blood perfusion within the prostate once the temperature field is obtained.

Thermal therapy for the BPH treatment is aimed to thermoablate the objective prostate tissue permanently while preserving the healthy tissue, especially the urethral wall. To optimize heating process, quantification of the tissue injury based on the temperature history is very important. Typical biophysical and biochemical events occurring in thermal injury at macro or cellular level have been discussed previously [25–27]. They include: thermal denaturation of proteins, alterations in metabolic process, thermally induced alterations in physical or chemical characteristics of cells such as hyperpermeability of membrane, intracellular ionic concentration and nuclear degradation, loss of birefringence properties in muscle and collagen, and loss of hemoglobin from red blood cells. Moritz and Henriques [28] originally assumed, and this later became the standard for thermal injury evaluation, that the kinetics of the destruction process in living tissues is similar to the first-order chemical reaction process. Thus, if the damage function is defined as $\Omega(t)$, then the damage rate can be expressed as the Arrhenius formulation:

$$\frac{d\Omega}{dt} = P \exp\left(-\frac{\Delta E}{RT}\right) \tag{28}$$

where P is a constant corresponding to chemical reaction frequency, ΔE and R are the activation energy and universal gas constant, T is the absolute temperature. P and ΔE are normally obtained through curve-fitting the experimental data. But for different types of tissue in various temperature ranges, P and ΔE can be quite different [26,29,30]. The analysis of thermal damage has been recently advanced by considering the denaturation of enzyme protein under elevated temperature [31]. In a latest experimental study on membrane injuries, Bhowmick and Bischof [27] obtained the P and ΔE values for rat's Dunning AT-1 prostate tumor cells. Future experimental data for human tissues can be very useful for determining the effectiveness of thermal therapy.

The process of thermal injury takes place quickly and often occurs at the early stage of heating. Accurate predictions on the temperature evaluation during thermal therapy are expected to be critical for the treatment planning. Since prostatic tissue temperature increase results from the combined effects of blood perfusion, the heating power, and the coolant parameters, an effective therapy requires optimization of all these parameters to achieve certain degree of thermal injury in target tissue. The present analytical solution for the temperature distribution can be directly substituted into Eq. (28) to simplify the optimization procedure.

Although the real shape of the prostate is not exactly cylindrical, good agreement between the theoretical prediction and experimental measurement indicates that the approximation is reasonable for tissue outside the periurethral region and in the near field of the microwave antenna. The individual effects of arteries and veins in the vascular plexus surrounding the prostatic urethra on the tissue temperature were not considered in this study. Instead, the lumped effect of these vessels was incorporated into the overall heat transfer coefficient. Nevertheless, the simulation results have shown that accurate predictions can be achieved in the parenchymal region without considering the vessel effects as the $h = 257$ W/m^2·°C used is for the catheter only [12]. This can be mainly attributed to the fact that the periurethral arteries and veins are inter-wound and the net thermal effect of these vessels can be negligible in the far remote region in the radial direction. However, the nearly perfect heat exchange between the artery and vein can substantially enhance the tissue conduction in the z direction [32]. This anatomical structure virtually prevents the urethra from being thermally damaged during the heating. To model heat transfer accurately in this highly vascularized region, coupled energy equations need to be developed for the tissue and blood flow in the arteries and veins, which is beyond the scope of this paper. Finally, it is worth noting that at higher heating levels, periodic changes in blood perfusion triggered by natural thermoregulation in the body have been observed, which induced tissue temperature oscillations [20]. Under these conditions, a time-dependent perfusion term needs to be incorporated into the Pennes equation for accurate modeling in future. Once the vascular damage occurs at a temperature higher than 45°C, the vascular thermoregulation gradually diminishes. Low or nearly zero blood perfusion in tissue can result from further thermal damage. In such a case, tissue temperature can rise rapidly beyond 60°C without convective cooling of the blood. Heat would then transfer predominantly via conduction in tissue.

Acknowledgments

This work was supported by grant No. 7 R29 CA 67970-04 from the National Institutes of Health.

Nomenclature

c = specific heat of tissue, J/kg·°C
c_b = specific heat of blood, J/kg·°C
C_t = scale constant, mm$^{-0.8}$
h = heat convection coefficient, W/m^2·°C
k = thermal conductivity of tissue, W/m^2·°C
L = prostate length, m
N = coefficient
q''' = specific absorption rate, W/m^3
q^* = overall spatial heating, W/m^3

q_m = metabolic rate of tissue, W/m^3
Q = microwave power, W
r = radial distance, m
R_0 = radius of urethra, m
R_1 = radius of periurethral region, m
R_2 = outside radius of prostate, m
t = time, s
T = tissue temperature, °C
T_0 = initial temperature, °C
T_a = artery temperature, °C
T_∞ = body core temperature, °C
T_f = cooling water temperature, °C
z = axial position, m
z_0 = critical axial decay length, m
ξ, η, λ = coordinates correspond to r, θ, z
κ = coefficient
τ = time corresponds to t
ω_b = blood perfusion rate, ml/s/ml
ε = attenuation constant, mm^{-1}
ρ = density of tissue, kg/m^3
ρ_b = density of blood, kg/m^3
Δ = transformed temperature, °C
θ = angular coordinate, deg

References

[1] Astrahan, V. W., Sapozink, M. D., Cohen, D., Luxton, G., Kampp, T. D., Boyd, S., and Petrovich, Z., 1989, "Microwave Applicator Transurethral Hyperthermia of Benign Prostatic Hyperplasia," Int. J. Hyperthermia, **5**, pp. 283–296.

[2] Baert, L., Ameye, F., Willemen, P., Vandenhove, J., Lauweryns, J., Astrahan, M. A., and Petrovich, Z., 1990, "Transurethral Microwave Hyperthermia for Benign Prostatic Hyperplasia: Preliminary Clinical and Pathological Results," J. Urol. (Baltimore), **144**, pp. 1383–1387.

[3] Bdesha, A. S., Bunce, C. J., Kelleher, J. P., Shell, M. E., Vukusic, J., and Witherow, R. O'N, 1993, "Transurethral Microwave Treatment for Benign Prostatic Hypertrophy: a Randomized Controlled Clinical Trial," Br. Med. J., **306**, pp. 1293–1296.

[4] Homma, Y., and Aso, Y., 1993, "Transurethral Microwave Thermotherapy for Benign Prostatic Hyperplasia: a 2-Year Follow-Up Study," J. Endourology, **7**, pp. 261–265.

[5] Larson, T. R., Bostwick, D. G., and Corica, A., 1996, "Temperature-Correlated Histopathologic Changes Following Microwave Thermoablation of Obstructive Tissue in Patients With Benign Prostatic Hyperplasia," Urol., **47**, pp. 463–469.

[6] Marteinsson, V. T., and Due, J., 1994, "Transurethral Microwave Thermotherapy for Uncomplicated Benign Prostatic Hyperplasia," Scand. J. Urol. Nephrol., **28**, pp. 83–82.

[7] de la Rosette, J. J. M. C. H., Froeling, F. M. J. A., and Debruyne, F. M. J., 1993, "Clinical Results With Microwave Thermotherapy of Benign Prostatic Hyperplasia," Eur. Urol., **23**, (suppl. 1), pp. 68–71.

[8] Sapozink, M. D., Boyd, S. D., Astrahan, M. A., Jozaef, G., and Petrovich, Z., 1990, "Transurethral Hyperthermia for Benign Prostatic Hyperplasia: Preliminary Clinical Results," J. Urol. (Baltimore), **143**, pp. 944–950.

[9] Martin, G. T., Haddad, M. G., Cravalho, E. G., and Bowman, H. F., 1992, "Thermal Model for the Local Microwave Hyperthermia Treatment of Benign Prostatic Hyperplasia," IEEE Trans. Biomed. Eng., **39**, pp. 836–844.

[10] Xu, L. X., Rudie, E., and Holmes, K. R., 1993, "Transurethral Thermal Therapy (T3) for the Treatment of Benign Prostatic Hyperthermia (BPH) in the Canine: Analysis Using Pennes' Bioheat Transfer," in: *Advances in Heat and Mass Transfer in Biotechnology*, ASME HTD-Vol. 268, pp. 31–35.

[11] Yuan, D. Y., Valvano, J. W., Rudie, E. N., and Xu, L. X., 1995, "2-D Finite Difference Modeling of Microwave Heating in the Prostate," in: *Advances in Heat and Mass Transfer in Biotechnology*, ASME HTD-Vol. 322/BED-Vol. 32, pp. 107–113.

[12] Zhu, L., Xu, L. X., and Chencinski, N., 1998, "Quantification of the 3-D Electromagnetic Power Absorption Rate in Tissue During Transurethral Prostatic Microwave Thermotherapy Using Heat Transfer Model," IEEE Trans. Biomed. Eng., **45**, pp. 1163–1172.

[13] Patel, U. H., and Babbs, C. F., 1993, "Development of a Rapidly Computable Descriptor of Prostate Tissue Temperature During Transurethral Conductive Heat Therapy for the Benign Prostate Hyperplasia," Med. Biol. Eng. Comput., **31**, pp. 475–481.

[14] Loyd, D., Karlsson, M., Erlandsson, B. E., Sjodin, J. G., and Ask, P., 1997, "Computer Analysis of Hyperthermia Treatment of the Prostate," Adv. Eng. Softw., **28**, pp. 347–351.

[15] Sturesson, C., and Engels, S. A., 1996, "Theoretical Analysis of Transurethral Laser-Induced Thermotherapy for Treatment of Benign Prostatic Hyperplasia: Evaluation of a Water-Cooled Applicator," Phys. Med. Biol., **41**, pp. 445–463.

[16] Bigler, S. A., Deering, R. E., and Brawer, M. K., 1993, "Comparison of Microscopic Vascularity in Benign and Malignant Prostate Tissue," Hum. Pathol., **24**, pp. 220–226.

[17] Nissenkorn, I., and Meshorer, A., 1993, "Temperature Measurements and Histology of the Canine Prostate During Transurethral Hyperthermia," J. Urol. (Baltimore), **149**, pp. 1613–1616.

[18] Xu, L. X., 1999, "New Development in Bioheat and Mass Transfer Modeling," in: *Annual Review of Heat Transfer*, Chang-Lin Tien, ed., X, Chap. 1, Begell House, New York.

[19] Ozisik, M. N., 1993, *Heat Conduction*, 2nd ed., Wiley New York.

[20] Xu, L. X., Zhu, L., and Holmes, K. R., 1998, "Thermoregulation in the Canine Prostate During Transurethral Microwave Hyperthermia, Part I: Temperature Response," Int. J. Hyperthermia, **14**, pp. 29–37.

[21] Arkin, H., Holmes, K. R., and Chen, M. M., 1986, "A Sensitivity Analysis of the Thermal Pulse Decay Method for Measurement of Local Tissue Conductivity and Blood Perfusion," ASME J. Biomech. Eng., **108**, pp. 54–58.

[22] Chato, J. C., 1991, "Fundamentals of Bioheat Transfer," in: *Thermal Dosimetry and Treatment Planning*, Gautherie, M., ed., Springer-Verlag, New York, Chap. 1.

[23] Xu, L. X., Zhu, L., and Holmes, K. R., 1998, "Blood Perfusion Measurements in the Canine Prostate During Transurethral Hyperthermia," in: *Annals of New York Academia of Sciences*, Diller, K. R., ed., 858, Chap. 2, pp. 21–29.

[24] Zhu, L., Xu, L. X., Yuan, D. Y., and Rudie, E. N., 1996, "Electromagnetic (EM) Quantification of the Microwave Antenna for the Transurethral Prostatic Thermotherapy," in: *Advances in Heat and Mass Transfer in Biotechnology*, ASME HTD-Vol. 337/BED-Vol. 34, pp. 17–20.

[25] Henriques, F. C., and Moritz, A. R., 1947, "Studies of Thermal Injury, I. The Conduction of Heat to and Through Skin and the Temperatures Attained Therein: A Theoretical and an Experimental Investigation," Am. J. Pathol., **23**, pp. 531–549.

[26] Pearce, J., Liao, W. H., and Thomsen, S., 1998, "The Kinetics of Thermal Damage: Estimation and Evaluation of Model Coefficients," in: *Advances in Heat and Mass Transfer in Biotechnology*, ASME HTD-Vol. 362/BED-Vol. 40, pp. 71–75.

[27] Bhowmick, S., and Bischof, J. C., 1998, "Supraphysiological Thermal Injury in Dunning AT-1 Prostate Tumor Cells," in: *Advances in Heat and Mass Transfer in Biotechnology*, ASME HTD-Vol. 362/BED-Vol. 40, pp. 77–78.

[28] Moritz, A. R., and Henriques, F. C., 1947, "Studies of Thermal Injury II: the Relative Importance of Time and Surface Temperature in the Causation of Cutaneous Burns," Am. J. Pathol., **23**, pp. 695–720.

[29] Diller, K. R., and Klutke, G. A., 1993, "Accuracy of the Henriques Model for Predicting Thermal Burn Injury," in: *Advances in Bioheat and Mass Transfer*, ASME HTD-Vol. 268, pp. 117–123.

[30] Torvi, D. A., and Dale, J. D., 1994, "A Finite Element Model of Skin Subjected to a Flash Fire," ASME J. Biomech. Eng., **116**, pp. 250–255.

[31] Xu, Y., and Qian, R., 1995, "Analysis of Thermal Injury Process Based on Enzyme Deactivation Mechanisms," ASME J. Biomech. Eng., **117**, pp. 462–465.

[32] Weinbaum, S., Jiji, L. M., and Lemons, D. E., 1984, "Theory and Experiment for the Effect of Vascular Microstructure on Surface Tissue Heat Transfer—Part I: Anatomical Foundation and Model Conceptualization," ASME J. Biomech. Eng., **106**, pp. 321–330.